12A4

Upslope Flow and Cumulus Development Over an Isolated, Heated Mountain: Observations and Simulations

J. Cory Demko
University of Wyoming, Laramie, Wyoming

1. INTRODUCTION

It is well-known that cumulus convection erupts almost daily close to solar noon over the mountains in the interior western United States during the summer. Most introductory meteorology textbooks display schematics of topographically-induced, thermally-forced circulations over mountains (e.g., Ackerman and Knox 2007, p.365; Aguado and Burt 2007, p.238). Even relatively simple numerical simulations have shown that under sufficient solar radiation forcing, weak stratification, and weak wind, a thermally-direct circulation develops over a mountain, with anabatic flow converging over the mountain.

The anabatic circulation may be hard to detect because of the intense mixing within the CBL. Convective turbulence may mix the anabatic momentum over a considerable depth, and the ascending flow in thermals is far stronger than the mountain-scale updraft due to net anabatic flow. The CBL develops as a result of a positive surface sensible heat flux, both over mountains and the surrounding plains. The CBL topography over complex terrain is poorly understood, but the afternoon CBL depth usually exceeds the mountain top height in the western United States during the warm season. If the CBL remains capped by a stable layer, the toroidal circulation remains contained within the CBL (e.g., Banta 1984). When the capping is weaker, and sufficient low-level moisture is present, this circulation can lead to orographic cumulus convection, and an unknown part of the mountain-scale circulation is carried up through cloud base and detrained at higher levels in the free troposphere. This vertical transfer is concentrated into a number of vigorous buoyant cumuli smaller in width than the mountain. Buoyant cumulus convection may enhance the mountain-scale convergence near the surface, and maturing convection may suppress the convergence (e.g., Raymond and Wilkening 1982). Thus several orographic cumulus growth cycles are possible in a single day, as has been observed (e.g., Zehnder et al. 2006).

Thermally-forced orographic convergence and associated deep convection are essential to warm-season precipitation and to surface-troposphere exchange in regions with complex terrain. Because the mountains that drive the localized CBL convergence and deep convection are often small compared to model resolution, their impact on surface precipitation and deep-tropospheric conditions is poorly predicted by current numerical weather prediction (NWP) models (e.g., Bright and Mullen 2002). Even NWP models of sufficient resolution to resolve the thermally-direct orographic circulations are challenged in their ability to simulate the surface fluxes and CBL development over complex terrain, and thus to predict the timing and intensity of ensuing thunderstorms (e.g., Yu et al. 2006).

The purpose of this observational study is to document the evolution and vertical profile of anabatic flow (and associated heat convergence) over an isolated mountain, to examine the flow's thermal forcing, and to relate the flow to orographic cumulus development. Sections 2 and 3 respectively discuss the data sources and analysis method. Observations are summarized in Section 4. Section 5 examines the forcing of anabatic flow and its relationship with cumulus convection and section 6 shows initial modeling results from Weather, Research, and Forecasting (WRF) simulations.

2. DATA SOURCES

The data used in this study were collected as part of the Cumulus Photogrammetric, In situ and Doppler Observations (CuPIDO) campaign during the 2006 monsoon season around the Santa Catalina Mountains (SCM) in southeast Arizona (Damiani et al. 2008)[1]. This mountain range has a horizontal scale of 20-30 km and a vertical scale of ~2000 m above the surrounding plains. Sixteen days were selected, each with orographic cumulus development, aircraft data, soundings, and surface meteorological data (see Table 1 in Damiani et al. 2008). We mainly examine data from the three of these 16 days with the best aircraft data. The University of Wyoming King Air (WKA) aircraft measured winds, state variables, and humidity at sufficient frequency to compute vertical fluxes. Mobile GPS Advanced Upper-Air Sounding System (MGAUS) sondes were released at 45-90 minutes intervals during WKA flights, from a location just upstream of the mountain top. Ten automated surface meteorological stations were positioned around the mountain (**Fig. 1**). All measured basic averages are used in this study. Temperature and humidity was measured at 2 m, wind at 10 m AGL. Four stations were located on sufficiently level and homogenous ground that surface heat fluxes could be computed using the eddy correlation method, from data at 7 m AGL. The 4-station, 30 minute average sensible and latent heat flux is denoted at *SH* and *LH*, respectively. We also use meteorological data from a tower located on Mt Bigelow on the SCM spine, and from an astronomical observatory on Mt Lemmon, the highest point of the SCM.

[1] All CuPIDO data are archived at http://www.eol.ucar.edu/projects/cupido/.

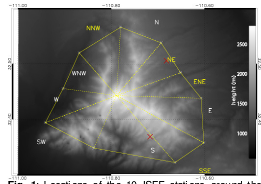

Fig. 1: Locations of the 10 ISFF stations around the Santa Catalina Mountains and the definition of the station polygon (solid yellow lines), based on mid-points between surface stations. The red crosses represent sounding launch sites (Windy Point near station S and Stratton Canyon at station NE).

meteorological variables at 1 Hz; five-minute

3. ANALYSIS METHOD

Both the flight patterns (circumnavigations) and the positioning of the surface stations around the SCM allow us to calculate the mountain-wide mass, heat, and moisture budgets. The method used here is similar to that used by Raymond and Wilkening (1980) for dry orographic circulations and Raymond and Wilkening (1982) for orographic cumulus. The mass convergence *MC* (kg m^{-1} s^{-1}) is defined as:

$$MC = \oint \rho v_n ds \qquad (1)$$

where v_n (ms^{-1}) is the wind component normal to the track, positive towards the mountain, ρ (kg m^{-3}) is the air density, and *ds* (m) is the incremental distance along the line integral. For aircraft data, 1 Hz data are used, giving a *ds* value of ~90 m. For station data, *ds* is the distance between the mid-points between stations (Fig. 1), and v_n the wind component normal to $d\vec{s}$ at the station between these midpoints. We then use the divergence theorem (Holton 2004; Johnson and Priegnitz 1981) to estimate the mean convergence within the aircraft loop or the station polygon (Fig. 1) with area *A* (m^2):

$$A^{-1}\oint v_n ds = -\nabla \bullet \vec{v}_h \qquad (2)$$

Here $\vec{v}_h$ is the horizontal wind vector. A convergence profile can be converted to a mean updraft $\overline{w}$ (ms^{-1}) within the loop:

$$\overline{w} = \frac{1}{Ag\rho_p}\int_p^{p_o}\left[\oint v_n ds\right]dp \qquad (3)$$

This assumes anelastic continuity and $\overline{w} = 0$ at the surface. The integral bounds are the surface pressure p_o and the flight level pressure *p* (Pa). The area A is computed as the sum of the areas of triangles defined by a base *ds* and a corner at Mt Lemmon. These triangles are shown in Fig. 1 for the station polygon area. The area is 576 km^2 for the station polygon, and about 739, 399, and 219 km^2 for the 300 m AGL, 780 hPa, and 700 hPa WKA loops around Mt. Lemmon.

The mean inflow $\overline{v}_n$ (m s^{-1}), referred to as the anabatic flow speed, is computed as follows:

$$\overline{v}_n = \frac{1}{C}\oint v_n ds \qquad (4)$$

where $C = \oint ds$ is the loop length, ranging from 52 km for the inner loop (700 hPa loop) to 102 km for the outer loop (300m AGL loop).

The mean (advective) wind $\vec{v}_m$ is defined as the vector mean wind along the track. Its magnitude will be compared to $\overline{v}_n$, to assess whether the flow primarily passes over/around the mountain, or is drawn towards the mountain.

We aim to quantify the horizontal flux convergence of mass and energy over the mountain, and place this in the context of changes in moist static energy over the mountain. Moist static energy *h* is defined as $h \equiv \pi\theta + gz + L_v q$, where Δ is the Exner function (J kg^{-1} K^{-1}),

$$\pi = c_p \, T/\theta = c_p\left(p/p_o\right)^{R/c_p}, \qquad (5)$$

c_p (J kg^{-1} K^{-1}) is the specific heat under constant pressure, *R* (J kg^{-1} K^{-1}) the ideal gas constant for dry air, p_o=1000 hPa, θ (K) the potential temperature, *T* (K) the temperature, *g* (ms^{-2}) gravity, *z* (m) height, L_v (J kg^{-1}) the latent heat of condensation, and *q* (kg kg^{-1}) the specific humidity. The conservation equation of *h*, for inviscid flow, implies (e.g., Batchelor 1967, equation 3.1.16):

$$\frac{\partial \rho h}{\partial t} + \nabla\cdot(\rho h\vec{v}) = S \qquad (6)$$

Here ρ(kg m^{-3}) is air density, $\vec{v}$ the 3-D wind vector, and *S* (W m^{-3}) is a diabatic heat source other than due to condensation/evaporation, e.g.

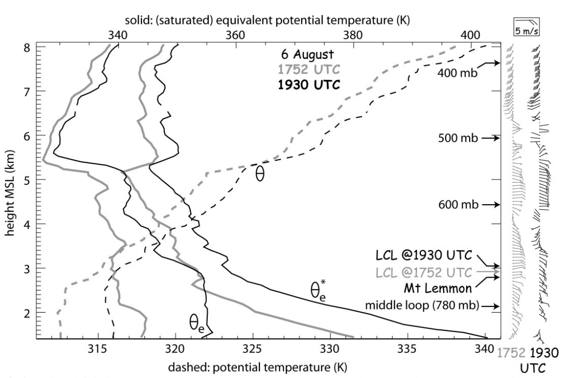

Fig. 2: Profiles of θ, θ_e, θ_e* and wind at 1532 UTC (grey) and 2000 UTC (black) on 06 August 2006. The data are derived from a MGAUS sonde released at Stratton Canyon at 1390 m MSL on the east side of Mt. Lemmon. The lifting condensation level (LCL) is shown for both soundings, as well as the elevation of Mt Lemmon. To see more detail in the profile of relatively weak winds, two full barbs are set to correspond with 5 m s^{-1}, double the standard convention.

radiative heat convergence. Integration of (6) over area A gives:

$$\iint_A \frac{\partial \rho h}{\partial t}dA = \oint \rho h v_n ds - \iint_A \frac{\partial \rho h w}{\partial z}dA + \iint_A S dA \qquad (7)$$

The first term on the right of (7) is the horizontal flux convergence. This line integral, derived using the 2-D divergence theorem, is computed over the closed loop defined by the station polygon (Fig. 1) or the WKA flight loops. This term is not preceded by a minus sign because the line-normal flow v_n is defined as positive towards the mountain. The second term on the right in (7) denotes the vertical flux convergence. Substitution of the definition of *h* in (7) yields:

$$\underbrace{\iint_A \frac{\partial(\rho h)}{\partial t}dA}_{I} = \underbrace{\oint \pi\rho\theta v_n ds}_{II} + \underbrace{\oint L\rho q v_n ds}_{III} + \underbrace{\oint g\rho z v_n ds}_{IV} - \underbrace{\iint_A \frac{\partial(\rho h w)}{\partial z}dA}_{V} + \underbrace{\iint_A S dA}_{VI} \qquad (8)$$

According to (8), the net change of moist static energy (I) expressed per unit volume over the mountain equals (II) the horizontal convergence of sensible heat, (III) the horizontal convergence of latent heat, (IV) the horizontal convergence of potential energy, (V) the vertical flux convergence of *h*, and (VI) any diabatic heat sources. Terms II and III are controlled by *MC*, slightly modulated by variations in temperature and water vapor respectively along the track. Term IV is negligible if the average height of the stations or of the aircraft along the flight loops is set to zero. Term VI is mainly due to surface sensible and latent heating mixed into the CBL. This term typically is far smaller than the horizontal heat convergences (terms II and III) near the surface. But in a control volume centered over the mountain, horizontally confined by the surface stations and vertically confined by a capping layer above the CBL (Fig.1), the net horizontal heat convergence is far smaller in magnitude than that either near the surface or that in the upper CBL. Thus a net change in *h* (term I) in the CBL over the mountain may be dominantly affected by the surface heat flux (term VI). In this paper, we examine the surface heat flux (term VI) and the horizontal convergence (terms II and III). We only display horizontal mass convergence (*MC*), inferred from surface and aircraft data, because terms II and III are essentially proportional to *MC*.

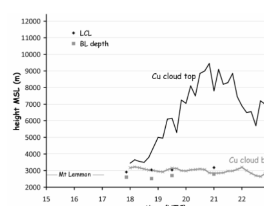

Fig. 3: Evolution of the depth of orographic cumuli over the SCM on 06 August. Also shown are the height of the mountain, the lifting condensation level (LCL) and the depth of the convective BL. The latter two are inferred from the MGAUS soundings. The LCL is computed assuming an air parcel mixed adiabatically in the lowest 500 m.

4. CASE STUDY OF MASS CONVERGENCE

We now illustrate the evolution of mass and moisture convergence and cumulus growth for 06-August during CuPIDO. In order to compare $\overline{v}_n$ values and resulting mass and energy convergence values from aircraft data with those from station data, the station data are low-pass filtered to 20 minutes, the time needed to complete the WKA outer loop. The evolution of $\overline{v}_n$ and convergence is interpreted in terms of local surface heat fluxes and the profiles of stability and wind. We characterize static stability by considering profiles of θ_e and the saturated equivalent potential temperature (θ_e*), as in **Fig. 2**.

On 26 July an unusually wet spell started, with dewpoint values well above average (Damiani et al. 2008). 6 August was the first day since the start of this spell that the daily-mean surface dewpoint dipped below the climatological average and the early-morning sky was clear. The MGAUS soundings reveal mostly weak and variable winds (fig. 2) over the depth of the Cu congesti that formed over the mountain in the early afternoon (**Fig. 3**).

A sounding released during the Cu congestus growth phase reveals a CAPE value of just 720 J kg^{-1}, and essentially no convective inhibition (Fig. 2, 1930 UTC sounding). Two layers of potential instability were present at 1930 UTC, one above the CBL and one near 5.5 km

(a) (b) (c) (d)

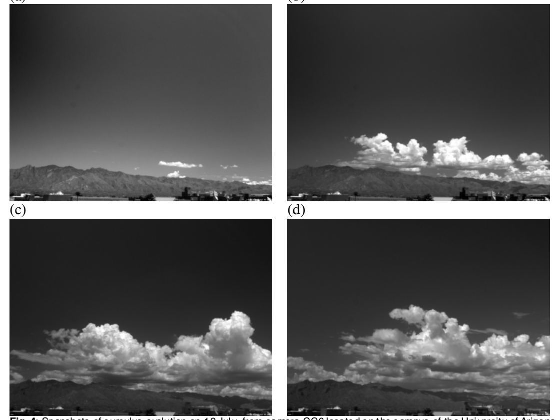

Fig. 4: Snapshots of cumulus evolution on 19 July, from camera CC6 located on the campus of the University of Arizona, at (a) 1900 (b) 2010 (c) 2120 and (d) 2220 UTC.

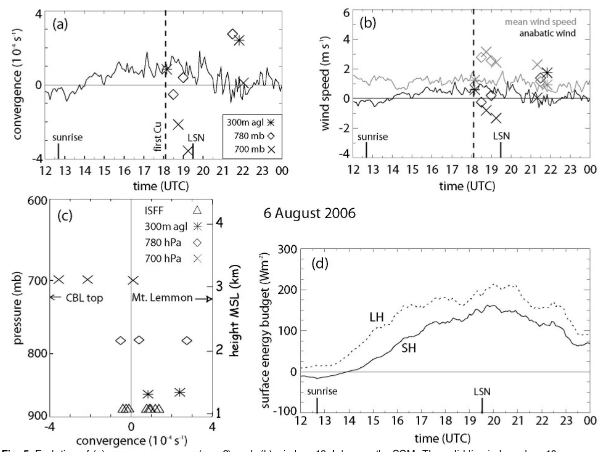

Fig. 5: Evolution of (a) mass convergence (eqn 2) and (b) wind on 19 July over the SCM. The solid line is based on 10 ISFF stations; the symbols apply to aircraft measurements at three levels. Sunrise, local solar noon, and time of first Cu are shown. In (b), both the anabatic wind (eqn 4) (black line and symbols) and the mean wind speed (grey line and symbols) are shown. (c) Mass convergence profile from surface and airborne measurements. The surface measurements represent 20 min averages at times corresponding to each of the aircraft loops. (d) Average surface sensible and latent heat flux for the four surface flux stations shown in Fig. 2.

MSL (Fig. 2). A weakly stable layer between 7 and 9 km MSL blocked further growth of the Cu congesti. The first orographic Cu formed fairly late (1800 UTC) (**Fig. 4**a), and the cloud tops grew gradually over the course of three hours (Fig. 4b, c, and d). No lightning or precipitation was recorded. Because of the high soil moisture around the mountain, the daytime *LH* exceeded *SH* (**Fig. 5**d). The CBL depth was not much below the LCL, and non-orographic BL cumuli developed in the afternoon, mainly east of the SCM (Fig. 4d).

Anabatic flow started rather early on this day, at about the same time as when *SH* became positive. In the early afternoon (21-23 UTC) the cloud top heights above Mt Lemmon waned (Fig. 3 and Fig. 4d). The last available sounding, at 21 UTC, does not reveal any mid-level drying or stabilization compared to previous soundings on this day, thus this cloud top decline must be related to boundary-layer processes: both the surface energy fluxes (Fig. 5d) and the mass convergence (Fig. 5a) decreased during this period; the latter even became negative.

Eight loops were flown around the mountain, all *after* the first orographic Cu. The outer and middle loops were within the CBL, the inner loops remained above the CBL (Fig. 5c). The five early loops (1750-1920 UTC), flown during the early Cu growth phase, indicate that the flow was convergent at low levels (consistent with surface observations during this period), non-divergent in the upper CBL (780 hPa), and divergent above the CBL (700 hPa). This is the strongest evidence yet for a toroidal circulation, partly contained within the CBL. During the Cu decay phase after 21 UTC, another stack was flown. Strong convergence was encountered at low and mid levels, in discordance with surface measurements and the observed Cu evolution.

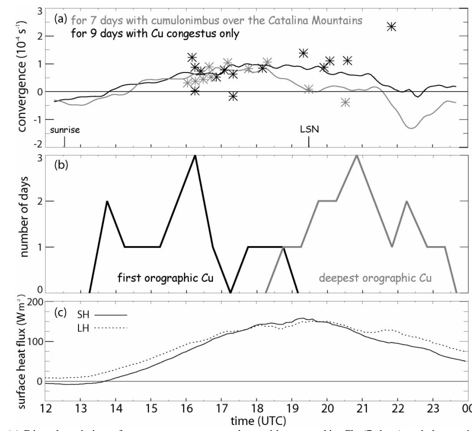

Fig. 6: (a) Diurnal variation of mass convergence on days with orographic Cb (7 days) and those with only Cu congestus development (9 days). The lines represent averages based on surface station data, and the symbols represent 24 loops flown at 300 m AGL. (b) Diurnal variation of the time of first Cu and of deepest Cu for the 16 flight days, inferred from the CC6 camera images. (c) Average surface heat fluxes for the same days.

5. THERMAL FORCING OF ANABATIC FLOW

a. *Orographic convergence and cumulus convection*

We now examine the signature of cumulus development on surface mass convergence for the 16 flight days. On each of these days orographic Cu developed, most commonly between 16-17 UTC (**Fig. 6**b), i.e. ~three hours before LSN. Orographic cumuli reached their maximum height most commonly in the first two hours after LSN, and their peak depth was at least 4 km, i.e. they became at least Cu congesti. The Cu grew to the cumulonimbus stage, with lightning recorded close to Mt Lemmon on 7 out of the 16 days (19 July, and 07, 09, 10, 11, 13 & 17 August).

During the 16 days, the WKA flew 24 loops around the mountain at 300 m AGL, all within the CBL, and all within 3.5 hours of LSN. The diurnal trend of mass convergence at the surface agrees well with the 24 convergence estimates from these flight loops (Fig. 6a), indicating that surface wind data alone are sufficient to estimate the convergence within the CBL. This is important because aircraft data are relatively expensive to collect, and the number of aircraft loops flown is insufficient to reveal the diurnal trend apparent in the 16 day record.

The composite convergence (Fig. 6a) suggests that no enhanced convergence was present in the hours before Cb development, and trends for individual days confirm this: the convergence on Cb days does not substantially exceed that on congestus-only days at any time. In fact over the course of the day, less surface convergence occurs on Cb days compared to congestus-only days. The one feature that distinguishes Cb days is that surface convergence generally vanished around LSN, with clear divergence after 22 UTC. High variability existed amongst the 7 Cb days and analysis of the individual days indicates that surface divergence generally developed shortly after the first lightning, suggesting cold pool development, as was observed in one case by Raymond and Wilkening (1982). Thus, while thunderstorms undoubtedly transport more CBL energy and moisture into the upper troposphere

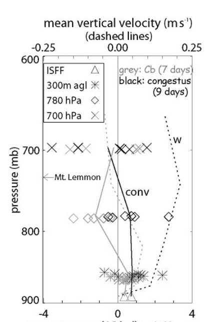

Fig. 7: Mass convergence profiles for the same days as in Fig. 6. The solid lines represent the average convergence profiles for Cb days and congestus days. The two ISFF measurements represent the time-averaged surface station measurements during the period of aircraft measurements, which occurred between 16 and 22 UTC. The dotted lines are vertical velocity (*w*) profiles derived from the convergence profile, assuming *w*=0 at the ground.

than Cu congesti, surface measurements suggest that *orographic thunderstorms suppress the BL solenoidal circulation*, due to cold-pool spreading.

The weakening of the solenoidal circulation by thunderstorms is confirmed by aircraft data. The 300 m AGL flight loops support the notion of afternoon divergence on Cb days (Fig. 6a). At the mid-level (780 hPa), divergence occurs on Cb days, and convergence on congestus-only days (**Fig. 7**). This is especially surprising since all but one 780 hPa loop on Cb days were flown before Cb occurrence. At 700 hPa no significant difference exists between Cb and congestus-only days. Mountain-scale vertical velocity (*w*) can be computed from the convergence values at various levels, using air mass continuity and assuming *w*=0 at the surface. On congestus-only days deep rising motion is present in the CBL, peaking at 0.21 ms^{-1} or ~750 m in one hour. Because of the slope of the terrain (about 0.10 between the ISFF stations and the mountain top), and the mean anabatic flow at the surface (0.4 ms^{-1} on average, during the period of the congestus-only flight loops, see Fig. 6a), the peak mountain-scale vertical velocity may be slightly higher, about 0.25 ms^{-1}. Orographic ascent in the CBL is weaker and shallower on Cb days (Fig. 7). Thus the aircraft data corroborate the conclusion reached from the surface data.

The two-month long record of ISFF data further corroborates that thunderstorms suppress the near-surface convergence: **Fig. 8** contrasts the composite mountain-scale convergence on days with thunderstorms (as determined by lightning occurrence within 13 km from Mt. Lemmon between 18-00 UTC, recorded by the National Lightning Detection Network) against that on days with shallow Cu over the mountain only (as inferred from CC6 time lapse photography). Clearly the solenoidal surface convergence is suppressed on Cb days, starting around LSN, while it is sustained through the afternoon on shallow Cu days. The mountain-scale convergence starts about 1 hour earlier and is more intense in the morning on Cb days, compared to shallow Cu days. The two-month record will be explored further in a separate study.

This conclusion is counterintuitive, yet it is not inconsistent with the aircraft data analysis by Raymond and Wilkening (1982). While the mean anabatic flow does converge moist static energy needed to *sustain* orographic convection, it may not explain the *onset* of orographic deep convection. In general deep convection is triggered where the CBL reaches the level of free convection, which is most likely where the CBL domes. Apparently this doming is not the result of the solenoidal circulation, but rather local surface heating. In terms of eroding the convective inhibition (CIN) and maximizing CAPE, the anabatic flow does not help: it is the nature of solenoidal forcing that anabatic surface flow advects cooler air and aims to destroy the horizontal difference of virtual potential temperature (θ_v) (Section 5.b). Thus, ignoring any horizontal moisture gradients, anabatic flow lowers the moist static energy,

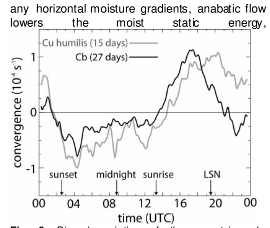

Fig. 8: Diurnal variation of the mountain-scale convergence, inferred from the 10-station polygon (Fig. 1), for 15 days with shallow orographic cumuli (grey line), and for 27 days with lightning over the SCM between 18-00 UTC (black line), between 22 June and 29 August 2006.

increases CIN, and decreases CAPE. This is consistent with the absence of enhanced anabatic flow prior to convective bursts, as discussed above.

The implications are twofold: (a) *mountain-scale mass convergence near the surface cannot be used as a precursor for convective initiation over mountains*, unlike in the plains (e.g., Wilson and Schreiber 1986; Wilson et al. 1992); and (b) *orographic cumulus vertical growth is controlled by* something else; the most likely candidate, as suggested by Zehnder et al. (2007), is *the evolution of the profile of static stability*, which is affected by surface heating over the mountain, or by changes aloft.

The composite surface data in Fig. 6a demonstrate that mountain-scale convergence develops about 1.5 hrs after sunrise, at about the same time as surface heating commences (*SH*>0, Fig. 6c). Such early start is typical for small-scale upslope flow [p. 179 in Whiteman (2000)], but it is earlier than expected for a mountain-plain circulation of this size. This is addressed further in Geerts et al. (2008). The convergence also peaks about 2 hrs before LSN (the time that *SH* peaks) on thunderstorm days (Fig. 6a, Fig. 8), about 1 hr before LSN on Cu congestus days, and about 1 hr after LSN for days with shallow Cu only (Fig. 8). This shift in peak convergence time confirms that moist convection suppresses the solenoidal circulation in the CBL.

These findings are based on a small sample and need to be further corroborated. In a separate study (in progress), we examine the relationship between cloud top evolution, moist static energy at Mt Bigelow, and mountain-scale convergence for the two-month period of ISFF data in CuPIDO, and statistically assess differences between different convective classes.

b. *Thermal forcing of anabatic flow*

We now examine the thermal forcing of the low-level anabatic wind and the toroidal circulation. Such circulation mostly contained within the CBL (low-level convergence, upper-level divergence) appears to be present on 6 August (Fig. 5c) as well as in the 16-day average profile (Fig. 7). The development of toroidal vorticity (η) around an isolated heated mountain is the result of solenoidal forcing, i.e. a gradient of buoyancy (or θ_v) towards the mountain:

$$\frac{D\eta}{Dt} \cong \frac{g}{\theta_v}\frac{\partial \theta_v}{\partial x} \tag{9}$$

Numerical simulations have documented the development of this baroclinicity and resulting circulation (e.g., de Wekker et al. 1998). Therefore we examine the variation of θ_v in a

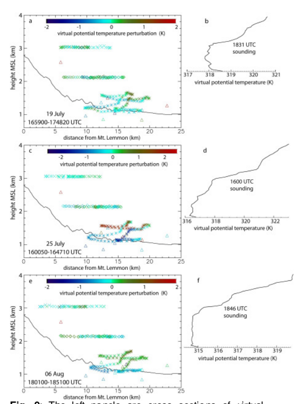

Fig. 9: The left panels are cross sections of virtual potential temperature θ_v, expressed as a perturbation from the mean value at any of the three flight levels or at the surface. Aircraft data from the three loops are shown with distinct symbols, and surface data are shown as triangles. The solid black line is an indicative, average terrain profile. The right panels show the θ_v profile from a sounding released around the time that the data in the left panels were collected. They have the same vertical axis as the left panels. The top, middle, and bottom panels are for 19 July, 25 July, and 6 August respectively.

vertical cross section on three days studied (**Fig. 9**). The terrain profile is an average in all four wind directions, starting at Mt. Lemmon. All aircraft and surface station data are plotted as a function of their distance from Mt. Lemmon. The vertical position of all data is their height MSL, rather than their height above the indicative terrain, because the solenoidal forcing needs to be evaluated on constant pressure surfaces. This places some surface stations ‘underground’. In most cases the upper flight loop data are collected above the CBL, as is evident from the θ_v profiles (Fig. 9b, d, and f). Thus, to reveal radial differences, θ_v perturbations are plotted. The perturbation θ_v is defined as the departure from the mean at any of the three flight levels, or from the mean of the 10 surface stations. Data from the Bigelow flux tower are included (the

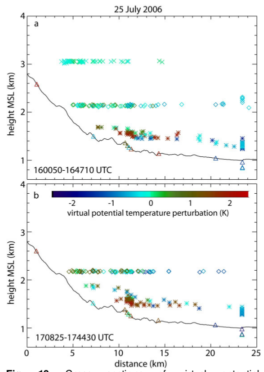

Fig. 10: Cross sections of virtual potential temperature θ_v based on aircraft and station data, for 25 July, for the period of (a) 1601-1647 UTC, and (b) 1708-1745 UTC. As in Fig. 9, the actual height MSL of the observations is shown, but unlike in Fig. 9, the x-axis value is the distance at which the actual height above the ground optimally corresponds with the height above the average terrain profile (black line) triangle at 2583 m MSL in Fig. 9.

For this site the perturbation θ_v is defined as the departure from the mean θ_v at the 780 hPa flight loop, because that flight level comes closest to the elevation of Mt Bigelow. The aircraft data were filtered to 10 seconds (~800 m along-track distance) and the 5-min station data were averaged to match the time needed to collect all aircraft data. The radial extent of the data is somewhat limited because of the flight patterns and the distribution of surface stations. Mt. Bigelow is on a ridge at 6.6 km to the southeast of Mt Lemmon, thus it appears much higher than the average terrain height.

One common aspect for the three cross sections in Fig. 9 is that Mt Bigelow has a ~2K higher θ_v than at the 780 hPa flight level, including on 19 July and 6 August, when the CBL top clearly was above the elevation of Mt. Bigelow. This is true also for other cross sections of combined multi-level aircraft data and station data (not shown), except one, on 6 August at 2113-2201 UTC, presumably because of a cold pool development associated with cloud top subsidence and divergent flow in the CBL. One may argue some instrument calibration problem at Mt. Bigelow, so we compared the Bigelow θ_v values to those just above the surface in soundings released from both Windy Point and Mt Lemmon (locations are shown in Fig. 1) at several times when the CBL was well-developed and deep. These values corresponded well. This yields evidence of *a warm core over the mountain.*

Otherwise, the aircraft and surface data do not reveal a clear pattern of warmer air ($\theta_v' > 0$) closer to the mountain. In essence, the station layout and flight pattern were not ideal to measure solenoidal forcing: a long line of stations and low-level, terrain-following flight tracks across the mountain would be superior. The large azimuthal asymmetry of θ on 25 July explains the large variations in θ_v' seen in Fig. 9c, especially for the lower, outer loop. Aircraft data give some indication for the expected baroclinicity on 6 August (Fig. 9e). This series of loops was flown later than the others and closer to LSN. Certainly the difference in observed surface convergence (not shown for 19 and 25 July) strength cannot be explained by differences in the θ_v' distribution (Fig. 9). We also plotted the data points at the observed height MSL, with their distance from Mt Lemmon determined by the condition that their plotted height above the average terrain profile equals the actual height AGL. This method redistributes the data and does reveal the expected baroclinicity more clearly, especially in two cross sections on 25 July (**Fig. 10**), when the anabatic flow was the strongest. Here the aircraft data suggest a radial θ_v gradient of roughly 1 K/(10 km), with warmer air closer to the mountain.

6. WRF SIMULATIONS

Detailed simulations using the Weather, Research and Forecasting, Nonhydrostatic Mesoscale Model (WRF-NMM) model have been conducted on 3 days (19 and 25 July and 06 August) during CuPIDO. Several modeling studies have been performed using idealized terrain to simulate the developing convergent flow over heated, elevated terrain (REFERENCES), however, lack the connection to observations and simulations over actual terrain. CuPIDO allows both and addresses issues such as how well WRF can accurately simulate the observed mountain-scale convergence and convective development? Also, what drives mountain-scale convergence and how does BL flow interact with orographic convection?

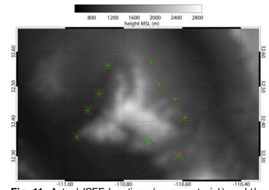

Fig. 11: Actual ISFF locations (green asterisk) and the closest WRF grid point (red diamonds) used for mountain-scale convergence measurements.

a. WRF initialization and validation

Using the 00 UTC NCEP North American Mesoscale 12 km grids for the respectable day and configurations specified in appendix A, WRF ran for a 36-hour forecast. In order to validate the model, we look at the WRF's convergent profile defined by the 10-sided polygon defined by the ISFF stations. Figure 11 shows the 10 ISFF stations and WRF's closest grid point to each station. From these points, a model, mountain-scale convergence can be computed using 10m winds. Figure 12 illustrates such measurements from two separate simulations for 06 August 2006. Two PBL schemes (Mellor-Yamada-Janjic (MYJ) and the Yonsei University) were chosen to illustrate the benefit of using one over the other. Figure 12 demonstrates no added advantage of using either PBL scheme; so for the remainder of discussion, simulations using the standard MYJ PBL scheme are examined. Figure 13 shows the ability of the WRF to accurately simulate the vertical structure of the atmosphere. Winds are primarily weak and from the south-southeast at the surface, veering towards the north above the PBL to 700 hPa then WSW from that point upward. The mid-level moisture present in the actual 12 UTC KTUS sounding is not present in the WRF and probably attributed to the radiosonde travelling through an alto-stratus deck.

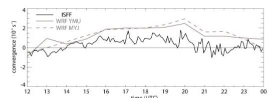

Fig. 12: Mountain-scale convergence measurement from the ISFF stations (black solid) and two WRF runs using the Mellor-Yamada-Janjic PBL scheme (grey dashed) and another using the Yonsei University scheme (grey solid) for 06 August 2006.

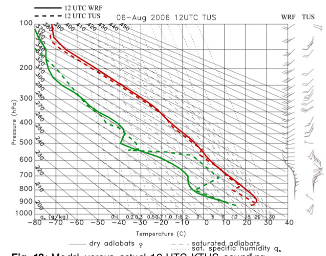

Fig. 13: Model versus actual 12 UTC KTUS sounding for 06 August 2006. Temperature profiles are illustrated in red and dewpoint profiles in green (dashed-actual and solid-WRF). Wind profiles are illustrated on the right (black-WRF and grey-actual).

b. Thermally-driven orographic flow

Observations show nocturnal, drainage flow becoming convergent between 13 and 15 UTC (figs. 5 and 6) as the surface warms and the surface layer couples with the residual layer from the previous evening. Figure 14 illustrates 2 m potential temperature and 10 m winds for forecast hours 12, 16, 20, and 24 on 06 August. Drainage flow exist in valleys and gullies around the SCM at 12 UTC. South to southwesterly winds along the ridgeline is most likely attributed to the mean flow at those levels and not drainage flow (see fig. 13). Four hours later (16 UTC) the surrounding valley warms by 4-6 K deepening the BL to over 1 km, therefore, eroding any hint of drainage flow near sunrise. Convergent flow commences on the NE side. The ridgeline still exhibits southwesterly flow still above the valley BL level. By 20 UTC, the BL deepens further over the valley and now analogous to the height of the ridgeline and convergent flow is obvious 10-15 km surrounding the mountain. The northwestern side and Bear Canyon, located southern periphery of the SCM, exhibits the strongest convergence. Weaker convergence due to wake flow around the SCM exists on the northeastern side. By 00 UTC 07 August, the BL has sufficiently warmed and vertical mixing has eliminated some of the convergence as evident by the westerly winds prevailing on the western side of the SCM. The strongest convergence at this time appears on the northeastern side due to the wake left behind the westerly surface flow. Figure 15 illustrates a composite view during which WRF develops the strongest convergence around the SCM (20 UTC). The black line in fig. 15b represents the cross section shown in (a)

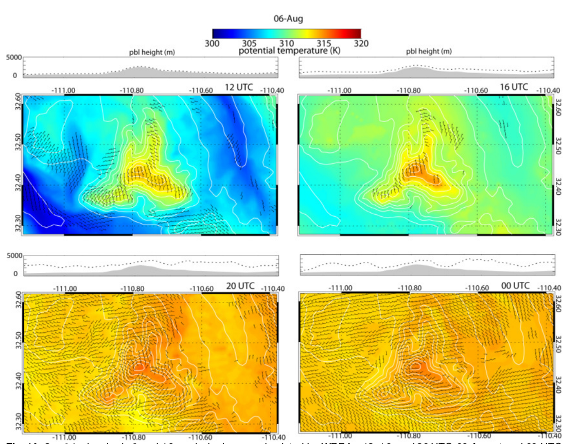

Fig. 14: 2 m θ (color shaded) and 10 m winds along as simulated by WRF for 12, 16, and 20 UTC 06 August and 00 UTC 07 August 2007. Boundary layer depth (dashed line) through and east-west cross section across Mt. Lemmon is also shown for the respectable time.

and (c). The cross section in (a) and (d) shows BL depth and the 2m θ and 10m winds with the center point being Mt. Lemmon represented by 0 km along the x-axis respectfully. Fig. 15c shows BL development and surface warming along with winds becoming convergent throughout the day. Once the BL top deepens over the lower terrain to the height of Mt. Lemmon winds become

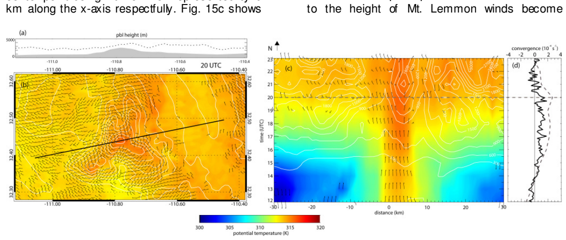

Fig. 15: Composite view during which WRF develops the strongest convergence around Mt. Lemmon. (a) Illustrates PBL depth along a 60 km cross section with the center being Mt. Lemmon. The cross section line is represented by the black line in (b). A plan-view of 2 m θ and 10 m winds showing maximum convergence 10-15 km around the SCM is shown in (b) and the same is shown in (c) along with BL depth contours through the same cross section as in (a). Mountain-scale WRF (grey-dashed) and ISFF (black-solid) convergence is illustrated in (d).

noticeably convergent starting at 19 UTC, specifically on the western side. Also shown in (c) is the warm core which develops slightly downwind (northeastern side) over the higher terrain. This warm core has been documented in several studies most notably Raymond and Wilkening (1980 and 1982) and Chen and Nash (1994), and in modeling studies such as Orville (1964), de Wekker et al. (1998), Kimura and Kuwagata (1995), Tian and Parker (2003), and Zängl and Egger (2004). Due to this warming, the BL bulges upward slightly downwind as shown in (a). Model convergence closely resembles the ISFF measured convergence with flowing becoming convergent at 14 UTC and gaining strength as the morning continues and the surface becomes a heat source. After peaking at 20 UTC, convergence diminishes as the BL fully develops, the thermal gradient relaxes between the warm core located over the mountain and the surrounding valley, and the mean flow becomes dominant over the anabatic component (mean component not shown). Figure 16 illustrates the vertical profile of convergence as defined by the 10-sided surface polygon upward to 200 hPa. The 12-17 UTC convergence average (black line) shows strongest convergence at the surface linearly declining and becoming divergence near/slightly below the PBL average top of 820 hPa (or roughly 550 m AGL). Aircraft and surface observations on this date confirmed this profile (see fig. 5). The 18-23 UTC average (grey line) shows strengthening BL convergence as expected since, on average, surface convergence peaks near local solar noon (see

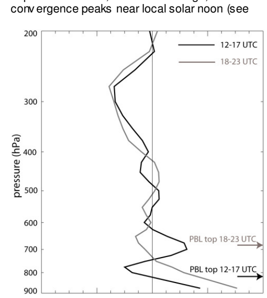

Fig. 16: Convergence profiles as computed from WRF on 06 August 2006. The black (grey) line represents the 12-17 UTC (18-23 UTC) average. The convergence area is defined by the midpoint-to-midpoint 10-sided surface polygon (ISFF station locations) up to 200 hPa.

fig. 6a and fig. 8). The 18-23 UTC profile linearly decreases with height, as does the 12-17 UTC, and the convergence becomes divergence at/slightly below the average PBL top located near 750 hPa (~2550 m AGL). Therefore, the WRF shows the solenoidal circulation is indeed contained within the PBL with the strongest inflow (convergence) occurring at the surface, becoming non-divergent generally 3/4 z_i and divergent (outflow) just below PBL top.

As discussed in section 5, solenoidal forcing implies a hydrostatic pressure difference between the mountain footprint and the surrounding air. Observations show (fig. 10) radial temperature gradient of roughly 1 K/(10 km), with warmer air closer to the mountain which supports the notion of a "warm dome" over the higher terrain. Figure 17 illustrates the radial potential temperature difference between Mt. Bigalow (2 m temperature approximately 2583 m ASL) and the surrounding pressure level (~750 hPa) for specific distances listed. Also plotted on the right axis is the corresponding PBL height (average) along the same compass direction. One should notice the distinct correlation between positive temperature differences (Mt. Bigalow's surface becoming warmer than surrounding distances at constant pressure) and PBL height. Once the PBL top over the corresponding radial locations becomes analogous to Mt. Bigalow, those locations now experience that pressure gradient force. The peak temperature difference generally occurs earlier on the east and south sides which intuitively makes sense as these surfaces are heated earlier and, therefore, peak earlier. Averaging all distances and directions yields a peak temperature difference between 19 and 21 UTC coinciding with the peak in surface convergence (fig. 6, 8, and 12). Fig. 17 also shows the greatest temperature difference occurring between 5 and 10 km from Mt. Bigalow; however still seen at 20 km suggesting the solenoidal forcing is strongest near the higher terrain and decreases further away. Figure 18 illustrates two-dimensional θ difference between specific surfaces and the surrounding pressure level. For example, fig. 18a shows θ difference between areas with a station pressure approximately 750 hPa (2m θ) and the corresponding pressure level (750 hPa θ). Figure 18b and c illustrates the same only for 800 and 850 hPa respectfully and 18d shows an east-west cross section of PBL height through Mt. Lemmon. Virtually all levels show a warm dome over the respectful pressure but none as large as 750 hPa. The prevailing winds at 800 and 850 hPa (fig. 18b and c respectfully) transports the warm dome downwind (winds not shown) yielding temperatures at or slightly below those at the same pressure. The warm dome bulging the PBL top over the mountain at the highest elevations

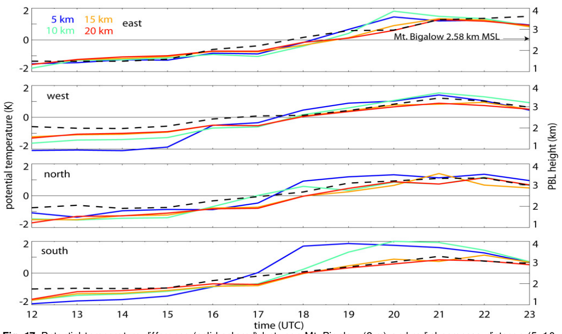

Fig. 17: Potential temperature difference (solid colored) between Mt. Bigalow (2 m) and radial compass distance (5, 10, 15, and 20 km) near the same pressure level (~750 hPa) for 20 UTC 06 August 2006. Average PBL height (dashed black) along the same distance and compass direction are illustrated on the right axis.

(~750 hPa) situates itself right over the mountain top due to weak winds (not shown) and non-divergent flow through the 10-sided polygon (fig. 16) occurring at 750 hPa. Whether this warm dome is the conduit between the surface anabatic flow and the lower free troposphere via cumulus development is unknown. Further WRF analysis on 06 August 2006 is needed.

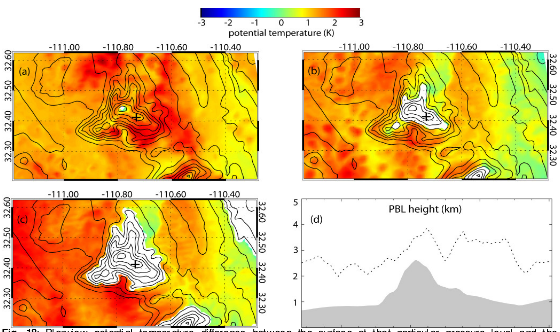

Fig. 18: Planview potential temperature difference between the surface at that particular pressure level and the surrounding constant pressure surface for (a) 750 hPa (b) 800 hPa and (c) 850 hPa for 20 UTC 06 August 2006. Panel (d) illustrates an east-west cross section through Mt. Lemmon of PBL height for the same time. The black cross indicates Mt. Bigalow.

7. Conclusions

Surface and aircraft data collected over the Santa Catalina Mountains in Arizona were used to study the development of mass and heat convergence over an isolated heated mountain, and their relation to orographic convection. This study focused on three days, and included an additional 13 days, each with Cu congestus or Cb development over the mountain. The main findings are as follows:

- Aircraft data collected along a closed loop around the mountain in the lower CBL indicate that mountain-scale convergence can be estimated well using data from a series of surface stations around the mountain.
- An orographic toroidal circulation with low-level anabatic flow and divergence near the CBL top is sometimes but not always present prior to orographic cumulus development.
- Station data indicate that mountain-scale convergence typically develops shortly after sunrise and peaks close to local solar noon. The anabatic flow is driven by surface heating over the mountain, resulting in solenoidal forcing and a hydrostatic horizontal pressure gradient force towards the mountain.
- Orographic cumulus and cumulonimbus development are not triggered by mountain-scale mass convergence near the surface, but rather probably by local surface heating; in fact convergent flow may suppress the initiation or deepening of convection over mountains. This does not mean that the low-level convergence of moist static energy by the anabatic flow is not essential for the maintenance of orographic convection. Surface flow tends to be katabatic following a thunderstorm outbreak over the mountain.
- WRF simulations show the ability to correctly diagnose the developing anabatic flow and resulting "warm dome" which develops over the Santa Catalina mountains; however, more analysis is needed to determine its role in orographic convection.

The 3rd and 4th conclusions will be corroborated in a follow-up study using two months of station data, collected as part of CuPIDO, and results will be stratified as a function of stability, thunderstorm development, and soil moisture.

References

Ackerman, S.A., and J.A. Knox, 2007: *Meteorology: Understanding the Atmosphere* (2nd edition). Thomson, 464 pp.

Aguado, E. and J.E. Burt, 2007: *Understanding Weather & Climate* (4th edition). Prentice Hall, 562 pp.

Banta, R. M., 1984: Daytime boundary-layer evolution over mountainous terrain. Part I: Observations of the dry circulations. *Mon. Wea. Rev.*, **112**, 340-356.

Batchelor, G. K., 1967: *An Introduction to Fluid Mechanics*. Cambridge Press, 615 pp.

Bright, D.R., and S.L. Mullen, 2002: Short-range ensemble forecasts of precipitation during the Southwest monsoon. *Wea. Forecasting*, **17**, 1080–1100.

Chen, Y.-L. and Nash A.J., 1994: Diurnal variation of surface airflow and rainfall frequencies on the island of Hawaii. *Mon. Wea. Rev.*, **122**, 34-56.

Damiani, R., J. Zehnder, B. Geerts, J. Demko, S. Haimov, J. Petti, G.S. Poulos, A. Razdan, J. Hu, M. Leuthold, and J. French, 2008: Cumulus Photogrammetric, In-situ and Doppler Observations: the CuPIDO 2006 experiment. *Bull. Amer. Meteor. Soc.,* **89**, 57–73.

de Wekker, S. F. J., S. Zhong, J. D. Fast, and C. D. Whiteman, 1998: A numerical study of the thermally driven plain-to-basin wind over idealized basin topographies. *J. Appl. Meteor.*, **37**, 606-622.

Geerts, B., Q. Miao, and J.C. Demko, 2008: Pressure perturbations and upslope flow over a heated, isolated mountain. *Mon. Wea. Rev.*, submitted.

Johnson, R.H., and D.L. Priegnitz, 1981: Winter monsoon convection in the vicinity of north Borneo. Part II: effects on large-scale fields. *Mon. Wea. Rev.*, 109, 1615–1628.

Kimura, F. and Kuwagata, T. 1995: Horizontal heat fluxes over complex terrain computed using a simple mixed-layer model and a numerical model. *J. Appl. Meteor.*, **34**, 549-558.

Orville, H.D., 1964: On mountain upslope winds. *J. Atmos. Sci.*, **21**, 622-633.

Raymond, D. J., and M. H. Wilkening, 1980: Mountain-induced convection under fair weather conditions. *J. Atmos. Sci.,* **37**, 2693-2706.

Raymond, D. J., and M. H. Wilkening, 1982: Flow and mixing in New Mexico mountain cumuli. *J. Atmos. Sci.,* **39**, 2211-2228.

Tian, W. and Parker, D.J. 2003: A modeling study and scalling analysis of orographic effects on boundary layer shallow convection. *J. Atmos. Sci.*, **60**, 1981-1991.

Yu, W., Y. Liu, T. Warner, R. Bullock, B. Brown, and M. Ge, 2006: A comparison of very short-term QPFs for summer convection over complex terrain areas, with the NCAR/ATEC WRF and MM5-based RTFDDA systems. Presented at the 7th WRF Users Workshop, 19-22 June, Boulder CO. (available at http://www.mmm.ucar.edu/wrf/users/workshops/WS2006/WorkshopPapers.htm)

Whiteman, C. D., 2000: *Mountain Meteorology: Fundamentals and Applications.* Oxford University Press, 376 pp.

Wilson, J. W., and W. E. Schreiber, 1986: Initiation of convective storms by radar-observed boundary-

layer convergent lines. *Mon. Wea. Rev.*, **114**, 2516–2536.

Wilson, J. W., G. B. Foote, N. A. Crook, J. C. Fankhauser, C. G. Wade, J. D. Tuttle, and C. K. Mueller, 1992: The role of boundary layer convergence zones and horizontal rolls in the initiation of thunderstorms: A case study. *Mon. Wea. Rev.*, **120**, 1785–1815.

Zängl, G. and Egger, J. 2005: Diurnal circulation of the Bolivian Altiplano. Part II. Theoretical and model investigations. *Mon. Wea. Rev.*, **133**, 3624-3643.

Zehnder, J.A., L. Zhang, D. Hansford, A. Radzan, N. Selover, and C.M. Brown, 2006: Using digital cloud photogrammetry to characterize the onset and transition from shallow to deep convection over orography. *Mon. Wea. Rev.*, **134**, 2527–2546.

Zehnder, J.A., J. Hu and A. Razdan, 2007: A stereo photogrammetric technique applied to orographic convection. *Mon. Wea. Rev*, **135**, 2265–2277.